Check for updates



ADVANCED MATERIALS
www.advmat.de

# Multifunctional 3D-Printed Pollen Grain-Inspired Hydrogel Microrobots for On-Demand Anchoring and Cargo Delivery

*Yun-Woo Lee, Jae-Kang Kim, Ugur Bozuyuk, Nihal Olcay Dogan, Muhammad Turab Ali Khan, Anitha Shiva, Anna-Maria Wild, and Metin Sitti**

**While a majority of wireless microrobots have shown multi-responsiveness to implement complex biomedical functions, their functional executions are strongly dependent on the range of stimulus inputs, which curtails their functional diversity. Furthermore, their responsive functions are coupled to each other, which results in the overlap of the task operations. Here, a 3D-printed multifunctional microrobot inspired by pollen grains with three hydrogel components is demonstrated: iron platinum (FePt) nanoparticle-embedded pentaerythritol triacrylate (PETA), poly N-isopropylacrylamide (pNIPAM), and poly N-isopropylacrylamide acrylic acid (pNIPAM-AAc) structures. Each of these structures exhibits their respective targeted functions: responding to magnetic fields for torque-driven surface rolling and steering, exhibiting temperature responsiveness for on-demand surface attachment (anchoring), and pH-responsive cargo release. The versatile multifunctional pollen grain-inspired robots conceptualized here pave the way for various future medical microrobots to improve their projected performance and functional diversity.**

## 1. Introduction

Magnetic mobile microrobots have become promising for targeted, controlled, localized, and minimally invasive cargo delivery and treatment of diseases at hard-to-access and deep human body sites.[1–10] Efforts have been made to the development and implementation of such mobile medical microrobots, including fabrication of soft robotic microdevices,[11,12] synthesis of biocompatible or responsive (adaptive) materials,[13–15] and strategies for locomotion inside the body.[16–22] A myriad of remotely controlled medical microrobots has been proposed to enable shape change, multifunctionality, and reconfiguration in response to different stimuli, such as magnetic fields,[23–27] temperature,[28,29] chemical,[30,31] light,[32] and ultrasound,[33,34] for diverse medical applications, such as target drug delivery, minimally invasive surgery, and remote sensing.[35,36] However, microrobot interaction with biological tissues, complex biofluidic environments, and overlap of multiple stimuli are major challenges toward their future medical applications.[37]

The operation of the untethered microrobots is limited in the human body, which is composed of complex physiological environments with a myriad of stimuli, which might trigger non-desired actuation with non-desired function.[38,39] Without decoupled multifunctionality (multifunctional structures), multi-input stimuli of the robot's responsive structures overlap each other, resulting in a partial loss of substantial functional capabilities.[40] In order to avoid the interrupted actuation, decoupling the multiple stimuli inputs is crucial by making each stimulus respond for a single function only. In addition to decoupling multifunctionality, achieving controllable attachment to soft biological tissues is essential for many target implementations, such as collecting bio-signals, applying electrical signals to nerves, and delivering drugs at targeted locations for given durations.[41–44] However, current designs of micro-scale robots have put more weight on steering and locomotion, so they possess relatively simple surface morphology and lack certain functions, such as tissue attachment ability.[45,46] Inspired by nature, there has been a wide range of biological materials with a variety of morphological structures, which have given us possible solutions to numerous engineering challenges.[47–50] Among them, pollen grain is emerging as an alternative to adhesive structures for targeted drug delivery applications due to their unique nanospike-like morphology and large inner cavity structure.[51–53] Despite the development of pollen grain-inspired material applications, a majority of the suggested structures have been made from natural pollen grain composed

Y.-W. Lee, J.-K. Kim, U. Bozuyuk, N. O. Dogan, M. T. A. Khan, A. Shiva, A.-M. Wild, M. Sitti
Physical Intelligence Department
Max Planck Institute for Intelligent Systems
70569 Stuttgart, Germany
E-mail: sitti@is.mpg.de

U. Bozuyuk, N. O. Dogan, M. Sitti
Institute for Biomedical Engineering
ETH Zurich
Zurich 8092, Switzerland

M. Sitti
School of Medicine and College of Engineering
Koç University
Istanbul 34450, Turkey

The ORCID identification number(s) for the author(s) of this article can be found under https://doi.org/10.1002/adma.202209812.

© 2023 The Authors. Advanced Materials published by Wiley-VCH GmbH. This is an open access article under the terms of the Creative Commons Attribution License, which permits use, distribution and reproduction in any medium, provided the original work is properly cited.

**DOI: 10.1002/adma.202209812**

of passive materials or a single responsive material, which limits their functional diversity.[54–57] Decoupling the functions is crucial for achieving successful targeted drug delivery. If the robot has neither mobility nor the ability to control the attachment, the drug delivery cannot be targeted. If the drug release is passive rather than active, the drug encapsulated in the robot loses concentration due to leakage during locomotion. Thus, the three functions (locomotion, attachment, and drug release) should be decoupled for successful targeted drug delivery.

Here, we report a multifunctional pollen grain-inspired hydrogel (MPH) robot for targeted active drug delivery and controllable attachment to biological tissues. We printed the 3D MPH robots (120 µm in diameter), composed of a temperature-actuated spherical-shaped shell for controllable attachment, a pH-responsive cargo releasing sphere structure, and a magnetic-actuated layer with spikes (**Figure 1**). The ferromagnetic and biocompatible iron platinum (FePt) nanoparticles encapsulated within the robot body were actuated and steered by external rotating magnetic fields, reaching up to a translational speed of 532 µm $s^{-1}$. Furthermore, the robot was designed to allow the outer shell of poly N-isopropylacrylamide (pNIPAM) to shrink down to 49% by increasing the temperature of the outer shell through a temperature-responsive approach, which enabled controllable attachment by on-demand spike exposure. Finally, poly N-isopropylacrylamide acrylic acid (pNIPAM-AAc) was introduced to perform a pH-responsive on-demand cargo release function. The MPH robot design conceptualized here establishes the proof of concept for executing multiple tasks within a single microrobot structure for various future medical robots for their advanced and decoupled multifunctionality.

## 2. Results and Discussion

For the realization of multifunctional microrobots with controllable tissue or other surface attachment, we selected pollen grain as a biological inspiration source with different stimuli-responsive materials for proof-of-concept demonstrations. Inspired by the special morphology of the contact elements from pollen grains, the MPH robots were generated using two-photon polymerization-based 3D microprinting.[58–60] As shown in Figure 1a, the MPH robot developed here consisted of three main components/layers: inner cargo carrier sphere, inner pollen grain-inspired spike structure, and outer shell. In order to fabricate the robot with such three layers (Figure 1b), pNIPAM-AAc was first printed to form an inner cargo carrier sphere structure that takes part in on-demand cargo delivery based on pH stimulus. Second, pentaerythritol triacrylate (PETA) with dispersed FePt nanoparticles was 3D printed with an accurate and precise alignment to generate spike-like structures inspired by the pollen spikes. Lastly, pNIPAM without the AAc unit was printed to form the outer shell that covers the spikes for the temperature-dependent response behavior. The shrinkage of the pNIPAM outer shell in response to temperature increase

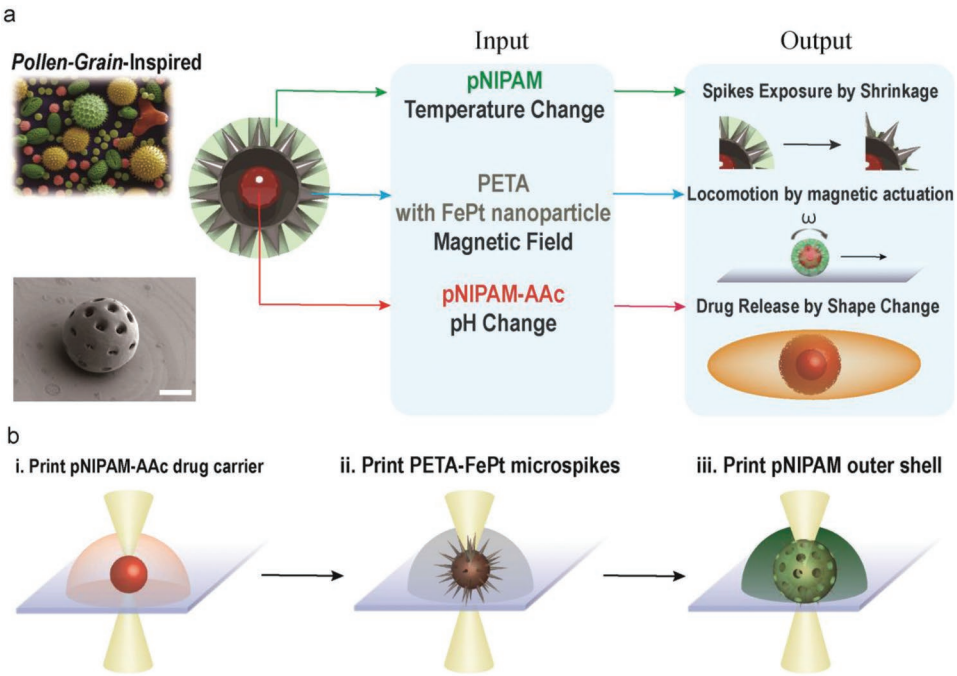



**Figure 1.** Multifunctional pollen grain-inspired hydrogel (MPH) robots for targeted drug delivery and on-demand tissue and other surface attachment. a) Schematic illustration of composition and operational principle of the MPH robot. 3D-microprinted MPH robots were composed of a temperature-actuated crust shell for controllable attachment, a pH-responsive cargo releasing sphere structure, and a magnetic actuated spike structure with pollen grain-inspired spikes. The integrated three different stimuli-responsive structures were actuated independently for their own functions. Scale bar: 50 µm. b) Schematic illustrations of the fabrication process of an MPH robot. The MPH robots are fabricated using a two-photon polymerization-based 3D microprinting technique. The active drug sphere is first printed with pNIPAM-AAc. After development, magnetically actuated pollen grain-inspired spike structures are printed using PETA with embedded FePt nanoparticles, and then the active outer crust shells are printed with alignment using pNIPAM hydrogel.


© 2023 The Authors. Advanced Materials published by Wiley-VCH GmbH

15214095, 2023, 10, Downloaded from https://onlinelibrary.wiley.com/doi/10.1002/adma.202209812 by Koc University, Wiley Online Library on [10/05/2023]. See the Terms and Conditions (https://onlinelibrary.wiley.com/terms-and-conditions) on Wiley Online Library for rules of use; OA articles are governed by the applicable Creative Commons License

15214095, 2023, 10, Downloaded from https://onlinelibrary.wiley.com/doi/10.1002/adma.202209812 by Koc University, Wiley Online Library on [10/05/2023]. See the Terms and Conditions (https://onlinelibrary.wiley.com/terms-and-conditions) on Wiley Online Library for rules of use; OA articles are governed by the applicable Creative Commons License

enabled on-demand attachment by revealing the PETA spikes. On the other hand, PETA with FePt particles only responded to magnetic fields, enabling rolling on biological surfaces with steering capability. Based on this decoupled actuation ability, the MPH robot could implement three different functionalities within a single microrobot structure: locomotion, on-demand surface attachment, and on-demand active cargo release in response to various independent stimuli.

Depending on the temperature of the outer shell, the MPH robot could select two different modes as shown in **Figure 2**a: the attachment mode by revealing the spikes over the outer shell, which enabled the robot to attach to the target position, and the locomotion mode by keeping the spikes under the outer shell, which enabled the robot to roll on the surface. Until now, existing microrobots were unable to alternate attachments to the surface. However, the MPH robot presented in this work could attach to the surface thanks to the shape-morphing ability of the MPH robot in a controlled manner. To explore the controllable attachment of the MPH robot, we investigated the temperature responsiveness of the outer crust shell made of pNIPAM hydrogel. We defined the shrinkage ratio ($\varepsilon$) of temperature-responsive crust structure as the ratio of the diameter change to the initial diameter of the crust structure as

$$\varepsilon\,(\%) = -\frac{l_0 - l}{l_0} \tag{1}$$

where $l$ and $l_0$ are the diameter of the shrunk and initial outer crust, respectively. The outer crust structures were fabricated by 3D microprinting, which was then transferred into the deionized water at room temperature. As a result of measuring the shrinkage ratio of the shells with respect to temperature

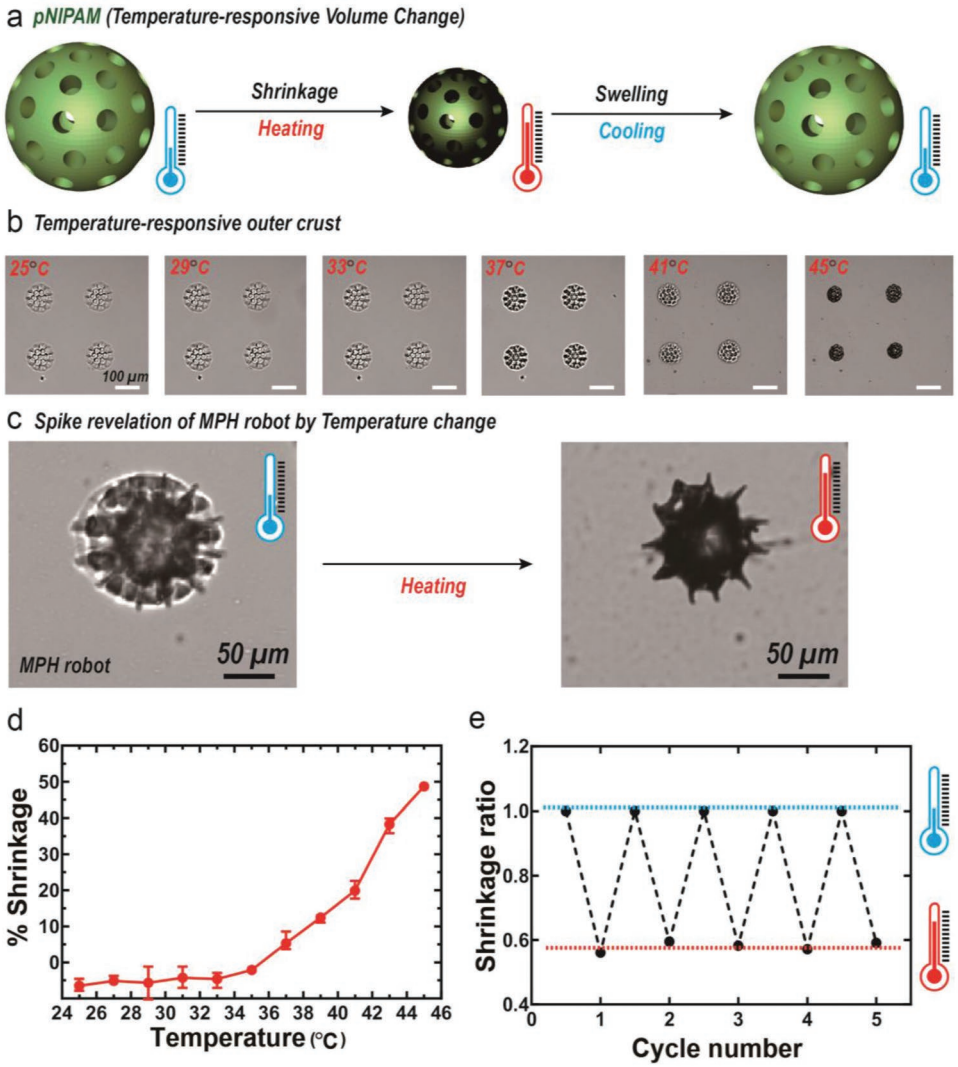



**Figure 2.** Temperature responsiveness of the size-controllable outer shell of the MPH robot. a) Schematic illustrations of temperature-induced shrinkage of the outer crust of MPH robot. b) Microscopic images showing real-time size changes for outer crust structures of pNIPAM hydrogels with temperature changes (25–45 °C). c) Optical images of the MPH robot with the controlled revelation of spike structures in response to temperature. d) Shrinkage ratio, defined as $-(l-l_0)/l_0$, with increasing temperatures for the pNIPAM hydrogels. e) The repetition test of the pNIPAM outer crust shrinking/unshrinking cycles without any deterioration.


© 2023 The Authors. Advanced Materials published by Wiley-VCH GmbH

from 25 to 45 °C, the pNIPAM showed a diameter shrinkage of ≈49% (Figure 2b–d). Hence, by integrating the spikes with the pNIPAM crust, the MPH robot could select either locomotion mode or attachment mode to construct controllable attachment. The temperature responsiveness of the outer crust of the robot could be explained by the unique behavior of pNIPAM. Hydrogels of pNIPAM typically undergo changes in their state by low critical solution temperature (LCST) behavior.[61–65] The pNIPAM structure expanded with the water absorption below its LCST because the polymer network of pNIPAM was in a hydrophilic state and the hydrophilic groups could interact strongly with water by hydrogen bonding when they were immersed in an aqueous solution. When the pNIPAM was heated above its LCST, the polymer network of pNIPAM became hydrophobic, expelling the water out of its network and thus shrinkage of the structure. This shrinking and unshrinking process could be repeated without deterioration as shown in Figure 2e. Nevertheless, the response time of the MPH robot to reveal the spikes was relatively long (≈20 min) due to the heat transfer method of hot air in this study. This might be further improved by alternating electric current using a coil setup.

When the MPH robot is attached to a biological surface for carrying out a task such as on-demand cargo delivery, the robot must remain on the surface despite external disturbances, such as biofluid flows. Hence, it is crucial to verify if the attachment of the robot is strong enough to withstand disruptions in various conditions. First, the drag and lift forces that the robot must resist in biofluids to remain on the surface of the biological channel were estimated by COMSOL simulations. Under the fully-developed laminar flow conditions with an average velocity of 5 cm $s^{-1}$ in a biological confined channel with a 1-mm inner diameter, the velocity magnitude around the MPH robot was much lower than the velocity at the center of the biological channel thanks to the small size of the robot (radius: 60 μm) compared to the diameter of the biological channel (**Figure 3**a–c). Thus, when the robot was attached to the channel, the lift and drag forces were only 0.008 μN and 0.204 μN, respectively (Figure 3d). Thanks to the lower drag force, it is postulated that the MPH robot can readily roll on the surface and anchor at the target spot even with flows against movement. However, depending on the robot's location, the drag force could be lower and the lift force could be even negative (Figure 3e,f). When the robot was located at the center of the biological channel, the lift force was zero while the drag force was the highest. As the robot approached the inner wall of the channel, the drag force decreased. However, the lift force increased until the robot reached a distance of 250 μm from the center line and then decreased beyond the distance. Furthermore, the lift force became negative when some part of the robot penetrated the inner wall of the biological channel, which means that the robot was pushed down to the inner wall of the channel. This is attributed to the fact that some part of the lower half of the robot doesn't experience the forces from the flow. Hence, the drag torque could contribute to a greater penetration force and allow for a more successful attachment to the surface. Based on these results, it could be concluded that the robot must resist the forces of at least sub-μN in both normal and tangential directions to remain on the surface in fluid environments, and the attachment force of the robot in the tangential direction is more important than the attachment force in the normal direction to stay still on the attached spot.

To analyze whether the robot could generate enough attachment performance and how effective the spike was in the attachment of the robot, the pull-off force and frictional force of the MPH robot were tested against various surfaces, such as synthetic silicone rubber and biological tissue surfaces. As shown in Figure 3g, the 7 × 7 printed spikes and outer shells of the MPH robot were prepared for the pull-off force and frictional force measurements, and the counterface sample (either Ecoflex 00–30 or porcine intestine) was used as a tip. When the spikes and outer shells were tested against the synthetic silicone surface, the spikes did not help to increase the pull-off force although they were marginally helpful to increase the frictional force regardless of the surface condition. In dry conditions, the spike sample showed ≈0.4-mN pull-off force and ≈3.7-mN frictional force while the shell sample showed ≈0.9-mN pull-off force and ≈3.3-mN frictional force in dry conditions (Figure 3h). Also, in wet conditions, the pull-off and frictional behaviors were the same, but the forces were significantly reduced to almost one-tenth of the measured forces in dry conditions. However, the spikes showed clear improvements in pull-off and friction forces against the porcine intestine as shown in Figure 3i. The outer crust shell sample showed ≈0.5-mN pull-off force and ≈0.7-mN frictional force, which were lower than the measured force values against the silicone sample in dry conditions. On the contrary, the spike sample showed ≈1.2-mN pull-off force and ≈2.8-mN frictional force, which were much higher than those from the shells. These results can be explained by the difference in mechanical properties between the silicone surface and the porcine intestine tissue surface as shown in Figure 3j. Since the silicone has high toughness and does not have any penetrable mucus on the surface, the spikes could not penetrate the surface, which resulted in less contact area than the shells. Thus, the spikes could not demonstrate a higher pull-off force than the shells. However, the spikes could generate a higher frictional force from the mechanical interlocking between the silicone surface and the spikes while the shells just slided on the surface. Nevertheless, the synthetic surfaces could easily be lubricated by applying water droplets at the interface, which resulted in reduction of pull-off and frictional forces of both the shells and the spikes. On the other hand, since the spikes can penetrate soft biological tissue surfaces,[66] the spikes could generate high pull-off and frictional forces compared to the shells, which cannot be explained without mechanical interlocking from penetration of the spikes. As for the attachment performance under the fluid flow disturbance, the spikes could provide strong attachment since the pull-off and frictional force values were tens of μN (49 robots with spikes can generate over 1 mN), which were much higher than the values obtained from the simulation (sub-μN). Although the high adhesive and frictional forces might decrease with a lower preload, the capillary force between the mucus layer and the robot surface or an external magnetic gradient provided by a strong permanent magnet could help to provide sufficient preload for attachment. In addition, Figure S1 (Supporting Information) clearly showed the effect of spikes on an attachment without maintaining an external normal load by demonstrating a strong attachment to biological tissue in a flow compared to the robot without the


© 2023 The Authors. Advanced Materials published by Wiley-VCH GmbH

15214095, 2023, 10, Downloaded from https://onlinelibrary.wiley.com/doi/10.1002/adma.202209812 by Koc University, Wiley Online Library on [10/05/2023]. See the Terms and Conditions (https://onlinelibrary.wiley.com/terms-and-conditions) on Wiley Online Library for rules of use; OA articles are governed by the applicable Creative Commons License

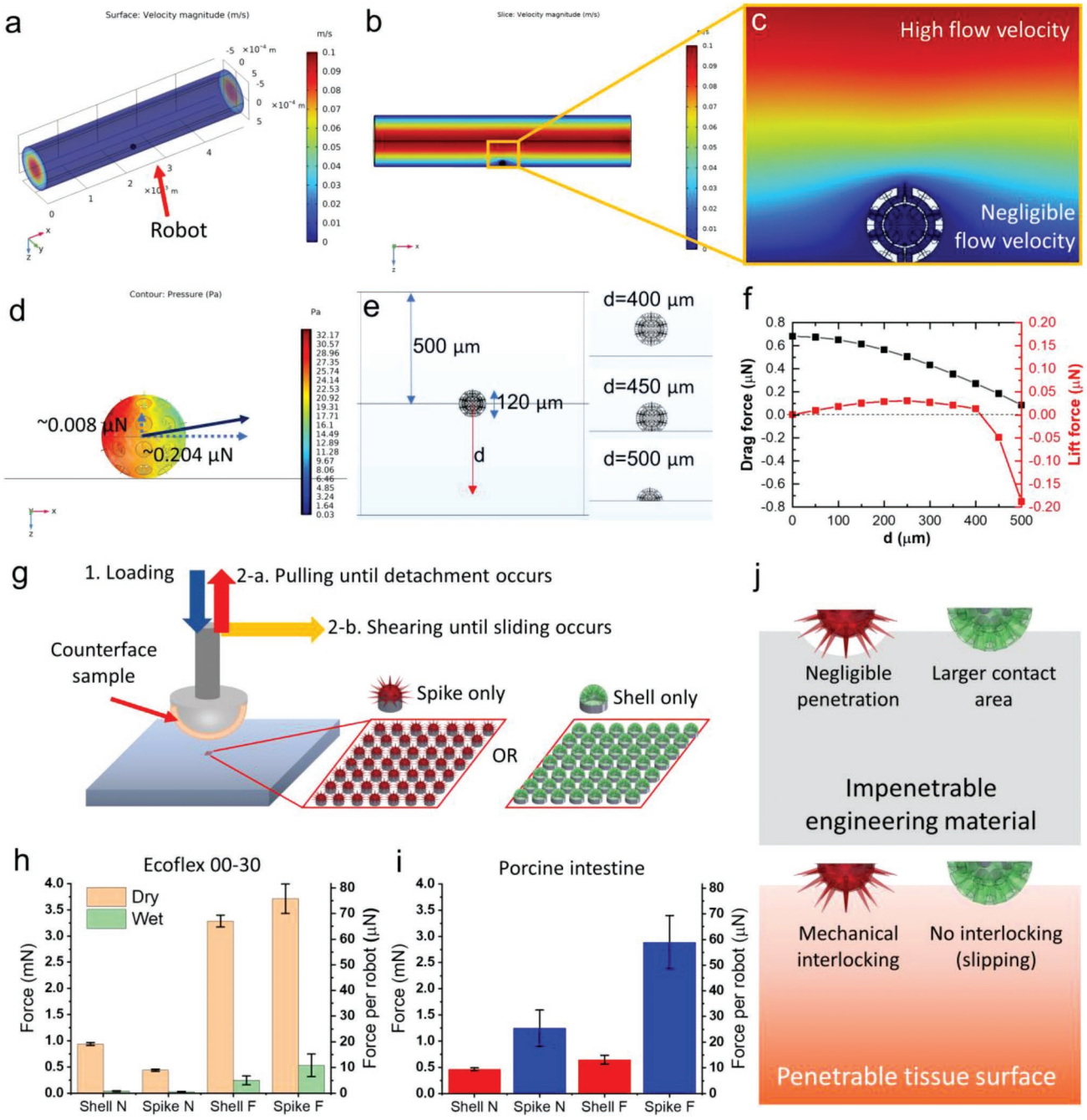



**Figure 3.** Anchoring performance of the MPH robot with controllable attachment a) COMSOL simulation for estimation of the drag and lift forces exerted on the MPH robot in a bloodstream (tube inner diameter: 1 mm, length: 5 mm). b,c) Velocity magnitude nearby the robot and its magnified image when the robot is attached to the surface of the vessel. d) Pressure distribution along the surface of the MPH robot, and the drag and lift forces acting on the robot. e) Images of the robot located at the distance, *d*, from the center line of the vessel. f) Drag and lift forces acting on the robot with respect to the distance from the center line to the robot. g) Schematic of pull-off force and frictional force measurement of the spikes and outer crusts from the robot. h) Pull-off force and frictional force measured from 49 spike-only robots and shell-only robots against Ecoflex 00–30 silicone surface in dry and wet conditions (Shell N and Shell F: Pull-off force and frictional force of the shell-only sample, respectively. Spike N and Spike F: Pull-off force and frictional force of the spike-only sample, respectively). Force per robot was obtained by dividing the measured force value by 49. i) Pull-off force and frictional force of 49 spike-only robots and shell-only robots against porcine intestine. j) Schematic of the attachment behavior of the spike and shell against silicone and soft tissue.

spikes. Hence, it can be concluded that the spikes of the robot can help attach to the surfaces in the human body by providing enough attachment performance despite external disturbances, especially against penetrable soft tissue surfaces.

In **Figure 4**a, we demonstrated the steering capability of the 3D-printed MPH robot to locomote by external magnetic actuation. For the locomotion of the MPH robot, we encapsulated FePt nanoparticles inside the PETA. The transmission electron


© 2023 The Authors. Advanced Materials published by Wiley-VCH GmbH

15214095, 2023, 10, Downloaded from https://onlinelibrary.wiley.com/doi/10.1002/adma.202209812 by Koc University, Wiley Online Library on [10/05/2023]. See the Terms and Conditions (https://onlinelibrary.wiley.com/terms-and-conditions) on Wiley Online Library for rules of use; OA articles are governed by the applicable Creative Commons License

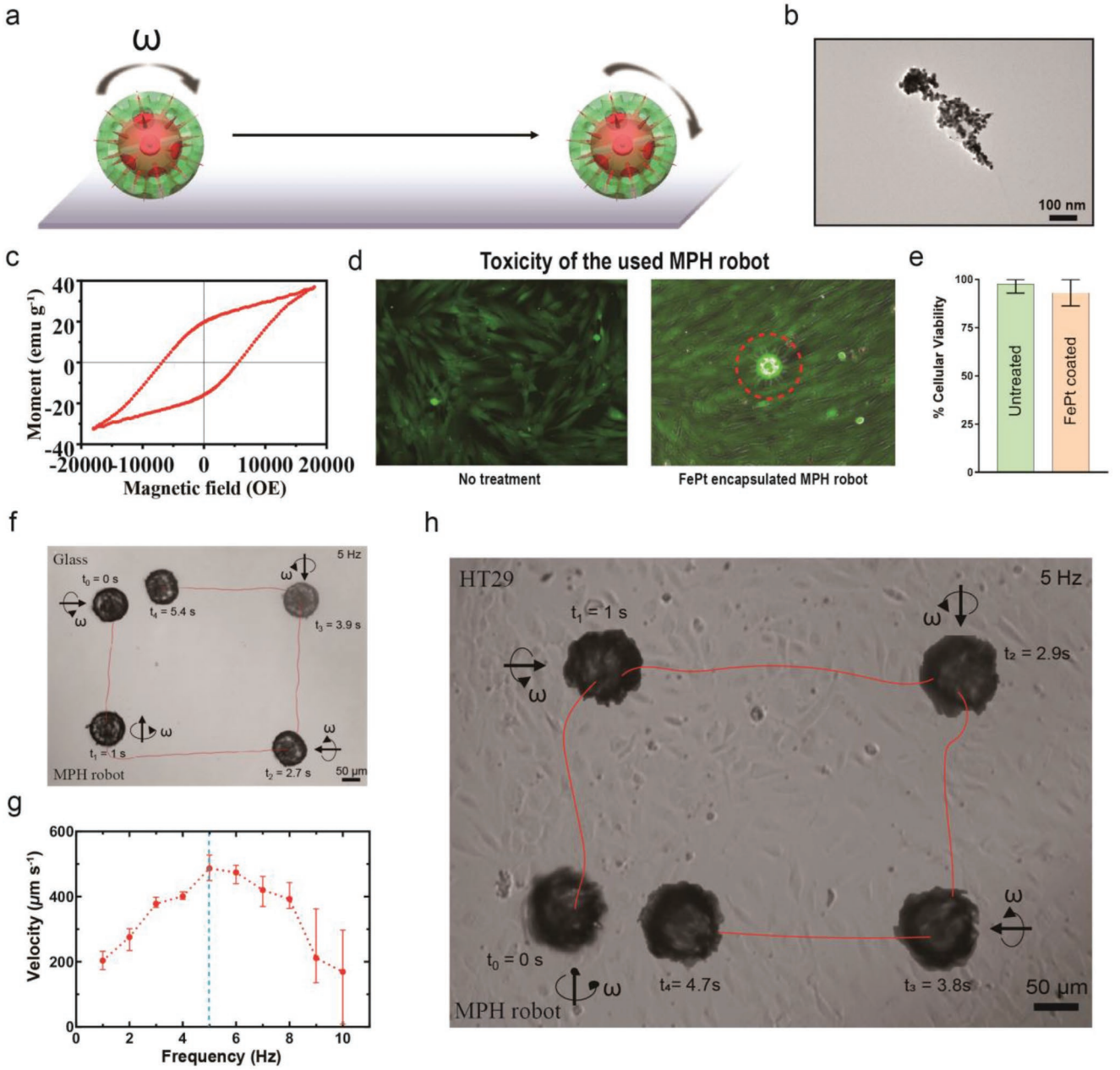



**Figure 4.** Magnetically guided locomotion of the FePt nanoparticle-embedded MPH robot. a) Schematic illustration of magnetic actuation and locomotion of the MPH robot. b) TEM image of the FePt nanoparticles. c) Magnetic hysteresis curve of the FePt nanoparticle-embedded MPH robot. d) The biocompatibility of the MPH robot assessed with human fibroblast cells at 48 h using live/dead staining. Green-live cells red-dead cells. e) The quantified amount of the cell viability of pollen robot compared to no treatment. f) Rolling trajectory of the MPH robot on a glass substrate g) Step-out frequency behavior characterization of the MPH robot. h) Demonstration of the MPH robot rolling locomotion on a cell (HT-29) monolayer surface without any interruption.

microscopy imaging revealed that the FePt nanoparticles had a sub-100-nm size in diameter (Figure 4b). The vibrating sample magnetometer analysis showed that the FePt nanoparticles had hard ferromagnetic characteristics with 36 emu $g^{-1}$ remanence magnetization, which is suitable for magnetic actuation.

Furthermore, we assessed the biocompatibility of the MPH robots to perform biomedical applications. We allowed human fibroblast cells to interact with the MPH robots for 48 h. At 48 h of incubation, we analyzed the biocompatibility of the structures with live/dead staining and metabolic activity measurements. The results indicated that the fibroblasts did not exhibit any toxicity-induced change (Figure 4d,e).

We analyzed the rolling locomotion behavior of the MPH robots further. We applied rotational magnetic fields with a custom-made electromagnetic setup mounted on an inverted optical microscope for these experiments.[67] The rotational magnetic fields actuated and steered the MPH robots by exerting torque in the direction perpendicular to their rotational


© 2023 The Authors. Advanced Materials published by Wiley-VCH GmbH

15214095, 2023, 10, Downloaded from https://onlinelibrary.wiley.com/doi/10.1002/adma.202209812 by Koc University, Wiley Online Library on [10/05/2023]. See the Terms and Conditions (https://onlinelibrary.wiley.com/terms-and-conditions) on Wiley Online Library for rules of use; OA articles are governed by the applicable Creative Commons License

15214095, 2023, 10, Downloaded from https://onlinelibrary.wiley.com/doi/10.1002/adma.202209812 by Koc University, Wiley Online Library on [10/05/2023]. See the Terms and Conditions (https://onlinelibrary.wiley.com/terms-and-conditions) on Wiley Online Library for rules of use; OA articles are governed by the applicable Creative Commons License

axis (Figure 4f,g). The roller-shape MPH robots converted the rotational behavior to translational movement due to the non-slip contact with the surface.[67] We also increased the applied frequencies stepwise, gradually increasing from 1 to 10 Hz to investigate the MPH robot's step-out frequency, which can be described as the point at which the robot starts to decrease its velocity. It was shown that the maximum forward velocity was 532 µm $s^{-1,}$ and the optimum actuation frequency (step-out frequency) was found at 5 Hz. Next, we investigated the motion of the MPH robot on the cellular substrate to confirm whether or not the robot possesses the capability to actuate and steer in biological environments. As shown in Figure 4h, the MPH robot could freely roll on the colon epithelial HT-29 cells without any disruption of the movement. Although the maximum velocity of 532 µm $s^{-1}$ at 5 Hz might be high enough to successfully approach the target spots, the translational speed is expected to be further improved by reducing the slip between the MPH robot and counterfaces or by improving the magnetic response of the embedded FePt particles. Other than that, closed-loop medical imaging-guided feedback mechanisms could also be implemented for improving controllability of the MPH robot.

To further improve the MPH robots by integrating the on-demand cargo release function, we introduced pH responsiveness by including acrylic acid (pNIPAM-AAc) in the precursor mixture before 3D direct laser printing. Carboxylic acid groups on the acrylic acid of pNIPAM-AAc can respond to pH stimulus by the transition in its protonated/deprotonated states. Hence, the spherical structure of the hydrogel network of pNIPAM-AAc changed its structure in response to the pH stimulus (**Figure 5**a). To further clarify this, we investigated pNIPAM-AAc spherical structures in different pH buffers from pH 3 to pH 11 (Figure 5b). The addition of varying pH solutions led to swelling/shrinking of the spherical structure up to 300% in the volumetric ratio of the structure (Figure 5c). The repetition

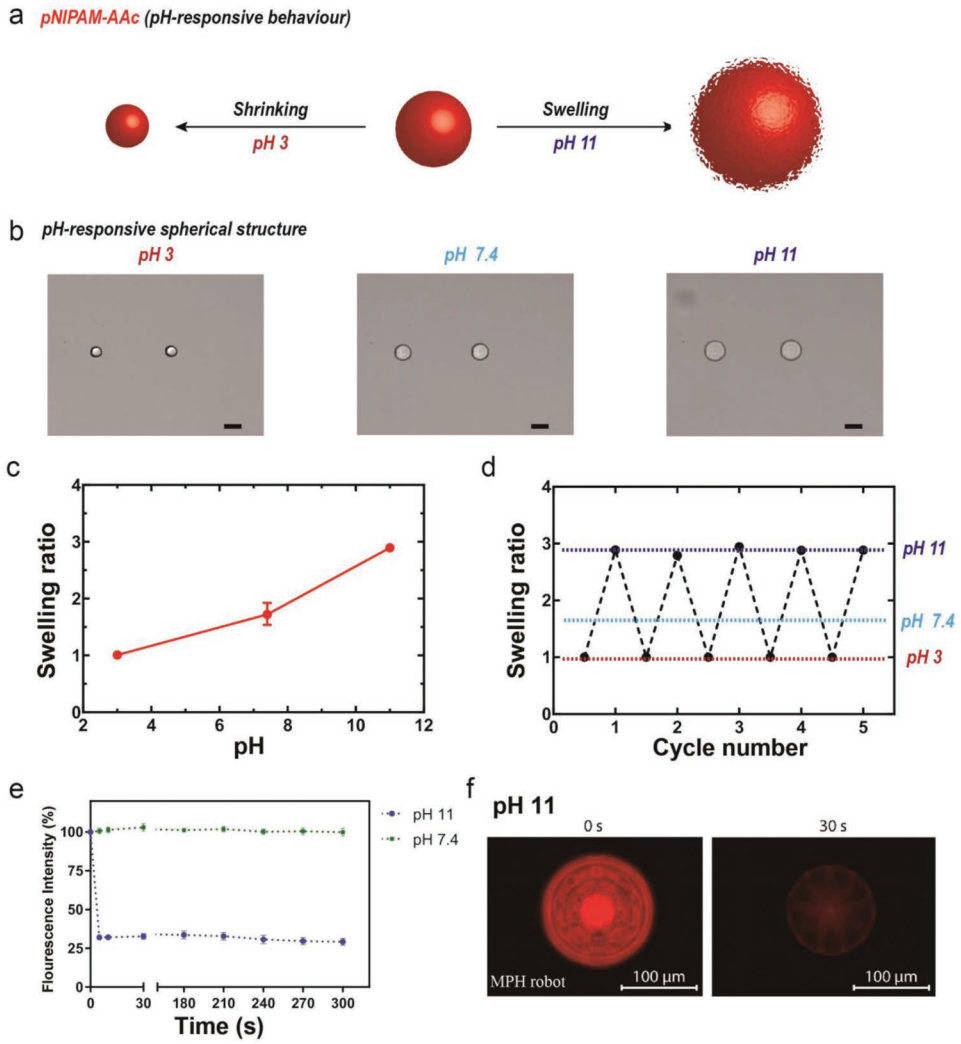



**Figure 5.** pH-responsive spherical structure of the MPH robot using pNIPAM-AAc. a) Schematic of the pH change-mediated drug release. b) Optical images showing the pH-responsive spherical structures. c) The swelling ratio for spherical patterns of pNIPAM-AAc hydrogels with pH change. d) The repetition test of the pNIPAM-AAc inner cargo carrier sphere swelling cycles in response to pH change. e) pH-mediated, structure swelling-driven drug release from the MPH robot. f) Fluorescence images of the drug-encapsulated MPH robot showing the drug release with pH-stimulated swelling behavior.


© 2023 The Authors. Advanced Materials published by Wiley-VCH GmbH

test for the swelling and the shrinking process was fully reversible at least during 5 cycles (Figure 5d), which demonstrates the superior repeatability of swelling/shrinking behavior of the MPH robot with high precision of the swelling ratio over cycles.

By utilizing the swelling of the pH-responsive pNIPAM-AAc inner drug carrier, the drug release test was carried out since on-demand therapeutic release is one of the challenges in medical microrobots for their targeted therapy. However, the drug-releasing mechanism of the existing pollen grain-inspired microrobots is passive, while those presented in this work can perform drug release actively since the MPH robot can respond to pH changes. Due to their porous hydrogel network, the pollen grain-inspired hydrogel adhesives presented here could provide a pH-responsive drug release function. As a representative of this potential, we explored the impact of pH stimulus on pollen grain-inspired hydrogel adhesives. We first loaded a fluorescent small-molecule drug analog, CellTracker Deep Red Dye, into the porous network of the pollen grain-inspired hydrogel attachment. To eliminate the effect of unstimulated stimulation, we first thoroughly washed the drug-loaded structures with Dulbecco's phosphate-buffered saline (DPBS) several times. Then, we introduced the pH 7.4 and pH 11 buffer solutions to the drug-loaded structures, where the release of the drug-analog molecule from the structures was measured by the fluorescent intensities inside the hydrogel network. When we exposed the structures to pH 11 buffer solution, we observed an immediate decrease in the fluorescent intensities due to the rapid swelling of the structures. As the structures swelled, the hydrogel size rapidly increased, and the encapsulated drug-analog molecules were released into the surrounding environment (Figure 5e,f). The response of the MPH robot was immediate to react within seconds, which is applicable for on-demand drug delivery functions. The release at pH 11 stopped, where 30% of the drug was still entrapped inside the hydrogel network. The uncompleted release could be explained by the molecular interactions between the drug molecules and the hydrogel network.[68] On the other hand, we observed no significant release at the pH 7.4 buffer solution since we did not observe swelling in this buffer solution (Figure 5e).

## 3. Conclusion

We have presented a strategy to fabricate multifunctional pollen grain-inspired hydrogel robots via 3D microprinting in order to enhance their functional diversity in biological/physiological environments. Due to the unique fabrication approach, we demonstrated multi-responsive hydrogel structures to decouple the stimuli inputs of magnetically actuated locomotion, temperature-responsive controllable attachment, and pH-responsive on-demand cargo release, respectively. The temperature-responsive outer crust shells made of pNIPAM enabled controlling the attachment of the microrobot by shrinking up to 49%, revealing the robot's spikes. In addition, the inner pollen grain-inspired structure with spikes made of PETA with FePt nanoparticles demonstrated an improved attachment performance and magnetically guided locomotion along biological surfaces. The inner sphere made of pNIPAM-AAc released drugs by pH-induced swelling. The proposed work here would be a groundwork to broaden the horizons of designing various medical robots and devices for implementing biomedical multifunctionality in the body.

## 4. Experimental Section

*Materials*: poly(*N*-isopropylacrylamide) (pNIPAM, Scientific Polymer Products Inc.), *N*-isopropylacrylamide (NIPAM, Scientific Polymer Products Inc.), acrylic acid (AAc, Sigma-Aldrich), *N*, *N*'-methylenebis-acrylamide (BIS, Sigma-Aldrich), Lithium phenyl-2,4,6-trimethylben zoylphosphinate (LAP, Tokyo Chemical Industry Co. Ltd.), pentaerythritol triacrylate (PETA, Sigma-Aldrich).

*Synthesis of pNIPAM and pNIPAM-AAc*: pNIPAM and pNIPAM-AAc solution was synthesized with the following recipe. A 3 g of NIPAM monomer, 0.4 g pNIPAM, and 0.17 g BIS were dissolved in 10 mL of ethylene glycol under stirring overnight (600 rpm) at 40 °C.

To this mixture solution, 310 µL of AAc (w/w) was added, followed by a 3% (w/w) LAP photoinitiator. The mixture was stirred (500 rpm) at 50 °C until all the components were mixed thoroughly.

*Synthesis of $L_{10}$ phase FePt nanoparticles*: FePt nanoparticles were synthesized as reported by Yu, Y. et al. with slight modifications to the protocol. Briefly, 0.2 mmol Pt(acac)2, 0.2 mmol Fe(acac)2, 0.8 mmol CTAC, and 0.5 ml oleic acid, were mixed with 10 ml oleylamine. The mixture was stirred under Argon gas for 1 h at room temperature. Afterward, the solution was heated to 350 °C at ≈5 °C $min^{-1}$. The mixture's temperature was kept constant at 350 °C for 3 h. Subsequently, the reaction mixture was cooled down to room temperature. FePt nanoparticles were precipitated by adding ethanol and centrifuged at 8000 rpm for 3 min. The particles were redispersed in hexane and again precipitated in ethanol, followed by centrifugation. This process was repeated at least five times to ensure the removal of the unreacted species and excess surfactants. The particles were then dispersed in hexane for storage and future use.

*Dispersion of particles in PETA*: Dried FePt (2 mg) nanoparticles were mixed with 1 ml of PETA and the photoinitiator mixture. A uniform dispersion was obtained using probe sonication for 1 min.

*Fabrication of Multifunctional Pollen Grain-Inspired Hydrogel Robot*: The cleaning process of glass substrates includes immersion in acetone and isopropyl alcohol and drying by nitrogen gas flow. The pNIPAM-AAc precursor mixture solution was dropped on a glass substrate for fabricating a pH-responsive sphere structure. A commercial Direct Laser Writing setup (Photonic Professional GT, Nanoscribe GmbH) with a 25X, NA = 0.8 oil immersion objective was used to print the pH-responsive sphere structures. The printing parameters are 50 mW of laser power and 50 000 µm $s^{-1}$ of scanning speed, respectively. After the first step of the printing, the spherical structures were developed with isopropyl alcohol for 30 min to remove the residue of pNIPAM-AAc. Then, FePt-loaded PETA prepolymer mixture droplet was dropped on the first printed structure. Laser power and galvanometric mirror *x*- and *y*-scanning speeds for FePt-loaded Peta structure were optimized to 80 mW and 50 000 µm $s^{-1}$, respectively. The second development was performed using isopropyl alcohol for 30 min to get high-quality 3D-printed submicron structures. To print the outer crust, the pNIPAM mixture solution was dropped on the spike structure. Printing parameters for the outer crust were optimized to a laser power of 60 mW and scanning speed of 50 000 µm $s^{-1}$. The design of MPH consisted spherical structure, spike, and an outer crust (120 µm in diameter).

*Characterization*: To analyze the samples in response to temperature and pH, a Nikon Eclipse Ti-E microscope at 10× and 20× magnification in the DIC mode was used for acquiring time-lapse images.

*Simulations*: COMSOL Multiphysics 6.0 simulation software (COMSOL, Inc.) was used to estimate the drag and lift forces exerted on the robot in the bloodstream in a blood vessel. A pipe with an inner diameter of 1 mm and a length of 5 mm was modeled and used as the blood vessel in the simulations. The robot model was directly imported from the 3D model for printing the robot in Nanoscribe. The


© 2023 The Authors. Advanced Materials published by Wiley-VCH GmbH

15214095, 2023, 10, Downloaded from https://onlinelibrary.wiley.com/doi/10.1002/adma.202209812 by Koc University, Wiley Online Library on [10/05/2023]. See the Terms and Conditions (https://onlinelibrary.wiley.com/terms-and-conditions) on Wiley Online Library for rules of use; OA articles are governed by the applicable Creative Commons License

bloodstream was designed to have an average velocity of 5 cm $s^{-1}$, a viscosity of 6 cP, and a density of 1060 kg $m^{-3}$. The flow conditions were determined based on the study of human blood.[69]

*Pull-off Force and Frictional Force Measurement*: A custom-built adhesion test setup was used to measure the pull-off and frictional forces. First, the 7-by-7 spikes and shells were prepared by using a two-photon polymerization-based 3D microprinter (Photonic Professional GT, Nanoscribe GmbH). Only the upper half of the spikes and shells with the 100-µm base were printed for the test. The spikes and shells were densely packed with a hexagonal pattern with a 200-µm interval. Second, a silicone sample (Ecoflex 00–30, Smooth-On Inc) or a porcine intestine sample were attached to a spherical tip and used as a counterface. After the sample was fixed in the test setup, the Load-Pull test for pull-off force and the Load-Drag test for frictional force were carried out. The counterface was moved to the spikes or shells until the normal load of 1 mN was achieved. Next, the counterface was pulled off with a 10 µm $s^{-1}$ retracting speed after 5 s of relaxation time for measuring pull-off force or was sheared to 500 µm at a shear rate of 10 µm $s^{-1}$ for measuring the maximum tangential force. For the wet condition with the silicone surface, several drops of deionized water were applied at the contact interface until the contact region was fully immersed in water.

*Cell Viability Studies*: The BJ fibroblast cell line (ATCC, CRL-2522) originating from healthy human foreskin tissue was used as the model cell line for cell viability studies. BJ fibroblasts were expanded in T-75 cell culture flasks containing Dulbecco's Modified Eagle's Medium (DMEM; Gibco) supplemented with 10% fetal bovine serum (Gibco) and 1% penicillin/streptomycin (Gibco). The detachment of cells was performed using trypsin (0.25 wt. %)/EDTA solution (Gibco) upon reaching 70% confluency.

For the biocompatibility assay, the cells were collected and seeded with a concentration of $1.5 \times 10^5$ each dish into 35 mm Petri dishes containing 9 MPH robot structures printed onto a glass slide. The positive control was treated with 20% DMSO (Sigma-Aldrich), and the negative control was kept untreated. All sample groups were performed in triplicates. The cells were incubated in an incubator at 37 °C in a humidified atmosphere of 5% $CO_2$ for 24, 48, and 72 h. The cell viability after exposure to the Pollen material was assessed using the LIVE/DEAD Cell Imaging Kit (Thermo Fisher Scientific, #R37601), which was performed according to the manufacturer's instructions. Fluorescence microscopy images were recorded using a Keyence BZ-X800E microscope. Live and dead cells were counted using the integrated hybrid cell count analysis module.

*Magnetic Actuation and Steering of MPH robot*: MPH robot was actuated and steered using our custom-made five-coiled electromagnetic setup, which could be mounted on an inverted optical Zeiss microscope. (Zeiss Axio Observer A1) The experiments were performed under a varied magnitude of rotating magnetic field. The step-out frequency was acquired by increasing the frequency of the rotating magnetic field from 0 to 10 Hz. The velocities of the MPH robot were calculated using an in-house open-access MATLAB code. For the experiments on biologically relevant cell surfaces, HT-29 colon epithelial cells were obtained from American Type Culture Collection (Rockville, MD, USA). The cells were cultured in Dulbecco's modified Eagle's medium supplemented with 10% (v/v) FBS, penicillin (50 UI $ml^{-1}$), and streptomycin (50 µg $ml^{-1}$) in a humidified, 37 °C, 5% CO2 environment. For the experiments, the cells were seeded on glass slides coated with fibronectin and waited for three days to reach confluence.

*pH-Responsive On-Demand Cargo Release*: For on-demand pH-responsive drug release experiments, the pH-responsive behavior of the robots was first checked by using only the inner sphere structure (Figure 5a–d). After ensuring the pH-responsive ability, the real drug release experiments were performed using the fully assembled structure of the robot. The structures were loaded with a 1 mM drug analog molecule (CellTracker Deep Red Dye, Invitrogen) overnight at 4 °C. After overnight incubation, the MPH robots loaded with drug analogs were washed several times with DPBS before the drug release experiments. The pH-responsive drug release experiments were conducted at pH 7.4 and pH 11. Briefly, the drug analog-loaded MPH robots were treated with different pH buffer solutions for 5 min. The time-lapse fluorescence intensities (bandpass emission: 670 nm) over at least three sphere structures were measured using the Nikon software for each pH value. Background fluorescence was subtracted from the measured values.

## Supporting Information

Supporting Information is available from the Wiley Online Library or from the author.

## Acknowledgements

Y.-W.L. and J.-K.K. contributed equally to this work. This work was funded by the Max Planck Society. Y.-W.L thanks the International Max Planck Research School for Intelligent Systems for the financial support. J.-K.K. thanks the Alexander von Humboldt Foundation for the fellowship support.

Open access funding enabled and organized by Projekt DEAL.

## Conflict of Interest

The authors declare no conflict of interest.

## Data Availability Statement

The data that support the findings of this study are available from the corresponding author upon reasonable request.

## Keywords

hydrogel microrobots, medical microrobots, multifunctionality, on-demand attachment, stimuli-responsive materials

Received: October 24, 2022
Revised: December 22, 2022
Published online: January 11, 2023

[1] A. Aziz, S. Pane, V. Iacovacci, N. Koukourakis, J. Czarske, A. Menciassi, M. Medina-Sánchez, O. G. Schmidt, *ACS Nano* **2020**, *14*, 10865.
[2] M. Cianchetti, C. Laschi, A. Menciassi, P. Dario, *Nat. Rev. Mater.* **2018**, *3*, 143.
[3] S. Fusco, M. S. Sakar, S. Kennedy, C. Peters, R. Bottani, F. Starsich, A. Mao, G. A. Sotiriou, S. Pané, S. E. Pratsinis, D. Mooney, B. J. Nelson, *Adv. Mater.* **2014**, *26*, 952.
[4] L. Hines, K. Petersen, G. Z. Lum, M. Sitti, *Adv. Mater.* **2017**, *29*, 1603483.
[5] W. Hu, G. Z. Lum, M. Mastrangeli, M. Sitti, *Nat.* **2018**, *554*, 81.
[6] K. L. Kozielski, A. Jahanshahi, H. B. Gilbert, Y. Yu, Ö. Erin, D. Francisco, F. Alosaimi, Y. Temel, M. Sitti, *Sci. Adv.* **2021**, *7*, eabc4189.
[7] C. S. X. Ng, M. W. M. Tan, C. Xu, Z. Yang, P. S. Lee, G. Z. Lum, *Adv. Mater.* **2021**, *33*, 2003558.
[8] M. Sitti, H. Ceylan, W. Hu, J. Giltinan, M. Turan, S. Yim, E. Diller, *Proc IEEE Inst Electr Electron Eng* **2015**, *103*, 205.
[9] B. Wang, K. Kostarelos, B. J. Nelson, L. Zhang, *Adv. Mater.* **2021**, *33*, 2002047.


© 2023 The Authors. Advanced Materials published by Wiley-VCH GmbH

15214095, 2023, 10, Downloaded from https://onlinelibrary.wiley.com/doi/10.1002/adma.202209812 by Koc University, Wiley Online Library on [10/05/2023]. See the Terms and Conditions (https://onlinelibrary.wiley.com/terms-and-conditions) on Wiley Online Library for rules of use; OA articles are governed by the applicable Creative Commons License

[10] Z. Wu, L. Li, Y. Yang, P. Hu, Y. Li, S.-Y. Yang, L. V. Wang, W. Gao, *Sci. Rob.* **2019**, *4*, eaax0613.
[11] H. Ceylan, I. C. Yasa, M. Sitti, *Adv. Mater.* **2017**, *29*, 1605072.
[12] J. Li, M. Pumera, *Chem. Soc. Rev.* **2021**, *50*, 2794.
[13] X. Hu, I. C. Yasa, Z. Ren, S. R. Goudu, H. Ceylan, W. Hu, M. Sitti, *Sci. Adv.* **2021**, *7*, eabe8436.
[14] Z. Ren, W. Hu, X. Dong, M. Sitti, *Nat. Commun.* **2019**, *10*, 2703.
[15] T. Wang, Z. Ren, W. Hu, M. Li, M. Sitti, *Sci. Adv.* **2021**, *7*, eabf7364.
[16] U. Bozuyuk, Y. Alapan, A. Aghakhani, M. Yunusa, M. Sitti, *Proc. Natl. Acad. Sci. USA* **2021**, *118*, e2022090118.
[17] N. O. Dogan, H. Ceylan, E. Suadiye, D. Sheehan, A. Aydin, I. C. Yasa, A.-M. Wild, G. Richter, M. Sitti, *Small* **2022**, *18*, 2204016.
[18] M. P. Kummer, J. J. Abbott, B. E. Kratochvil, R. Borer, A. Sengul, B. J. Nelson, *IEEE Trans Robot* **2010**, *26*, 1006.
[19] J. Li, X. Li, T. Luo, R. Wang, C. Liu, S. Chen, D. Li, J. Yue, S.-h. Cheng, D. Sun, *Sci. Rob.* **2018**, *3*, eaat8829.
[20] C. C. Mayorga-Martinez, M. Fojtů, J. Vyskočil, N.-J. Cho, M. Pumera, *Adv. Funct. Mater.* **2022**, *32*, 2207272.
[21] M. Medina-Sánchez, V. Magdanz, M. Guix, V. M. Fomin, O. G. Schmidt, *Adv. Funct. Mater.* **2018**, *28*, 1707228.
[22] I. C. Yasa, H. Ceylan, U. Bozuyuk, A.-M. Wild, M. Sitti, *Sci. Rob.* **2020**, *5*, eaaz3867.
[23] Y. Alapan, U. Bozuyuk, P. Erkoc, A. C. Karacakol, M. Sitti, *Sci. Rob.* **2020**, *5*, eaba5726.
[24] Y. Alapan, B. Yigit, O. Beker, A. F. Demirörs, M. Sitti, *Nat. Mater.* **2019**, *18*, 1244.
[25] U. Bozuyuk, E. Suadiye, A. Aghakhani, N. O. Dogan, J. Lazovic, M. E. Tiryaki, M. Schneider, A. C. Karacakol, S. O. Demir, G. Richter, M. Sitti, *Adv. Funct. Mater.* **2022**, *32*, 2109741.
[26] J. Giltinan, V. Sridhar, U. Bozuyuk, D. Sheehan, M. Sitti, *Adv Intell Syst* **2021**, *3*, 2000204.
[27] P. Wrede, O. Degtyaruk, S. K. Kalva, X. L. Deán-Ben, U. Bozuyuk, A. Aghakhani, B. Akolpoglu, M. Sitti, D. Razansky, *Sci. Adv.* **2022**, *8*, eabm9132.
[28] S. Palagi, A. G. Mark, S. Y. Reigh, K. Melde, T. Qiu, H. Zeng, C. Parmeggiani, D. Martella, A. Sanchez-Castillo, N. Kapernaum, F. Giesselmann, D. S. Wiersma, E. Lauga, P. Fischer, *Nat. Mater.* **2016**, *15*, 647.
[29] A. Pena-Francesch, J. Giltinan, M. Sitti, *Nat. Commun.* **2019**, *10*, 3188.
[30] X. Ma, A. C. Hortelão, T. Patiño, S. Sánchez, *ACS Nano* **2016**, *10*, 9111.
[31] X. Zhao, K. Gentile, F. Mohajerani, A. Sen, *Acc. Chem. Res.* **2018**, *51*, 2373.
[32] V. Sridhar, F. Podjaski, Y. Alapan, J. Kröger, L. Grunenberg, V. Kishore, B. V. Lotsch, M. Sitti, *Sci. Rob.* **2022**, *7*, eabm1421.
[33] A. Aghakhani, O. Yasa, P. Wrede, M. Sitti, *Proc. Natl. Acad. Sci. USA* **2020**, *117*, 3469.
[34] J.-F. Louf, N. Bertin, B. Dollet, O. Stephan, P. Marmottant, *Adv. Mater. Interfaces* **2018**, *5*, 1800425.
[35] B. J. Nelson, I. K. Kaliakatsos, J. J. Abbott, *Annu. Rev. Biomed. Eng.* **2010**, *12*, 55.
[36] F. Zhang, R. Mundaca-Uribe, N. Askarinam, Z. Li, W. Gao, L. Zhang, J. Wang, *Adv. Mater.* **2022**, *34*, 2107177.
[37] H. Ceylan, I. C. Yasa, U. Kilic, W. Hu, M. Sitti, *Prog. Biomed. Eng.* **2019**, *1*, 012002.
[38] F. G. Downs, D. J. Lunn, M. J. Booth, J. B. Sauer, W. J. Ramsay, R. G. Klemperer, C. J. Hawker, H. Bayley, *Nat. Chem.* **2020**, *12*, 363.
[39] Y. Wang, L. Shang, G. Chen, C. Shao, Y. Liu, P. Lu, F. Rong, Y. Zhao, *Appl. Mater. Today* **2018**, *13*, 303.
[40] Y.-W. Lee, H. Ceylan, I. C. Yasa, U. Kilic, M. Sitti, *ACS Appl. Mater. Interfaces* **2021**, *13*, 12759.
[41] J. Huang, Y. Liu, Y. Yang, Z. Zhou, J. Mao, T. Wu, J. Liu, Q. Cai, C. Peng, Y. Xu, B. Zeng, W. Luo, G. Chen, C. Yuan, L. Dai, *Sci. Rob.* **2021**, *6*, eabe1858.
[42] Y.-W. Lee, S. Chun, D. Son, X. Hu, M. Schneider, M. Sitti, *Adv. Mater.* **2022**, *34*, 2109325.
[43] Z. Ma, C. Bourquard, Q. Gao, S. Jiang, T. De Iure-Grimmel, R. Huo, X. Li, Z. He, Z. Yang, G. Yang, Y. Wang, E. Lam, Z.-h. Gao, O. Supponen, J. Li, *Stem Cells Int* **2022**, *377*, 751.
[44] M. P. Murphy, B. Aksak, M. Sitti, *Small* **2009**, *5*, 170.
[45] H.-W. Huang, F. E. Uslu, P. Katsamba, E. Lauga, M. S. Sakar, B. J. Nelson, *Sci. Adv.* **2019**, *5*, eaau1532.
[46] H. Lu, M. Zhang, Y. Yang, Q. Huang, T. Fukuda, Z. Wang, Y. Shen, *Nat. Commun.* **2018**, *9*, 3944.
[47] W.-G. Bae, H. Ko, J.-Y. So, H. Yi, C.-H. Lee, D.-H. Lee, Y. Ahn, S.-H. Lee, K. Lee, J. Jun, H.-H. Kim, N. L. Jeon, W. Jung, C.-S. Song, T. Kim, Y.-C. Kim, H. E. Jeong, *Sci. Transl. Med.* **2019**, *11*, eaaw3329.
[48] S. Baik, D. W. Kim, Y. Park, T.-J. Lee, S. Ho Bhang, C. Pang, *Nat.* **2017**, *546*, 396.
[49] A. L.e Duigou, G. Chabaud, F. Scarpa, M. Castro, *Adv. Funct. Mater.* **2019**, *29*, 1903280.
[50] V. Liimatainen, D.-M. Drotlef, D. Son, M. Sitti, *Adv. Mater.* **2020**, *32*, 2000497.
[51] T. Maric, M. Z. M. Nasir, N. F. Rosli, M. Budanović, R. D. Webster, N.-J. Cho, M. Pumera, *Adv. Funct. Mater.* **2020**, *30*, 2000112.
[52] R. C. Mundargi, M. G. Potroz, S. Park, H. Shirahama, J. H. Lee, J. Seo, N.-J. Cho, *Small* **2016**, *12*, 1167.
[53] M. Sun, Q. Liu, X. Fan, Y. Wang, W. Chen, C. Tian, L. Sun, H. Xie, *Small* **2020**, *16*, 1906701.
[54] S. Ito, S. N. Gorb, *ACS Appl. Mater. Interfaces* **2019**, *11*, 24691.
[55] D. Shin, W. T. Choi, H. Lin, Z. Qu, V. Breedveld, J. C. Meredith, *Nat. Commun.* **2019**, *10*, 1379.
[56] M. Sun, K. F. Chan, Z. Zhang, L. Wang, Q. Wang, S. Yang, S. M. Chan, P. W. Y. Chiu, J. J. Y. Sung, L. Zhang, *Adv. Mater.* **2022**, *34*, 2201888.
[57] T. Zhao, L. Yuan, T. Li, L. Chen, X. Li, J. Zhang, *ACS Appl. Mater. Interfaces* **2020**, *12*, 55362.
[58] M. Hippler, E. Blasco, J. Qu, M. Tanaka, C. Barner-Kowollik, M. Wegener, M. Bastmeyer, *Nat. Commun.* **2019**, *10*, 232.
[59] H. Jia, J. Flommersfeld, M. Heymann, S. K. Vogel, H. G. Franquelim, D. B. Brückner, H. Eto, C. P. Broedersz, P. Schwille, *Nat. Mater.* **2022**, *21*, 703.
[60] A. Sydney Gladman, E. A. Matsumoto, R. G. Nuzzo, L. Mahadevan, J. A. Lewis, *Nat. Mater.* **2016**, *15*, 413.
[61] J. C. Breger, C. Yoon, R. Xiao, H. R. Kwag, M. O. Wang, J. P. Fisher, T. D. Nguyen, D. H. Gracias, *ACS Appl. Mater. Interfaces* **2015**, *7*, 3398.
[62] L. Dong, A. K. Agarwal, D. J. Beebe, H. Jiang, *Nature* **2006**, *442*, 551.
[63] X.-J. Ju, L.-Y. Chu, X.-L. Zhu, L. Hu, H. Song, W.-M. Chen, *Smart Mater. Struct.* **2006**, *15*, 1767.
[64] P. M. Reddy, P. Venkatesu, *J. Phys. Chem. B* **2011**, *115*, 4752.
[65] C. Yoon, R. Xiao, J. Park, J. Cha, T. D. Nguyen, D. H. Gracias, *Smart Mater. Struct.* **2014**, *23*, 094008.
[66] Y. Wu, X. Dong, J.-k. Kim, C. Wang, M. Sitti, *Sci. Adv.* **2022**, *8*, eabn3431.
[67] A. Kaiser, A. Snezhko, I. S. Aranson, *Sci. Adv.* **2017**, *3*, e1601469.
[68] H. Ceylan, N. O. Dogan, I. C. Yasa, M. N. Musaoglu, Z. U. Kulali, M. Sitti, *Sci. Adv.* **2021**, *7*, eabh0273.
[69] E. Nader, S. Skinner, M. Romana, R. Fort, N. Lemonne, N. Guillot, A. Gauthier, S. Antoine-Jonville, C. Renoux, M.-D. Hardy-Dessources, *Front Physiol* **2019**, *10*, 1329.


© 2023 The Authors. Advanced Materials published by Wiley-VCH GmbH

15214095, 2023, 10, Downloaded from https://onlinelibrary.wiley.com/doi/10.1002/adma.202209812 by Koc University, Wiley Online Library on [10/05/2023]. See the Terms and Conditions (https://onlinelibrary.wiley.com/terms-and-conditions) on Wiley Online Library for rules of use; OA articles are governed by the applicable Creative Commons License